

Journal of Astronomical Telescopes, Instruments, and Systems

AstronomicalTelescopes.SPIEDigitalLibrary.org

Line spread functions of blazed off-plane gratings operated in the Littrow mounting

Casey T. DeRoo
Randall L. McEntaffer
Drew M. Miles
Thomas J. Peterson
Hannah Marlowe
James H. Tutt
Benjamin D. Donovan
Benedikt Menz
Vadim Burwitz
Gisela Hartner
Ryan Allured
Randall K. Smith
Ramses Günther
Alex Yanson
Giuseppe Vacanti
Marcelo Ackermann

Casey T. DeRoo, Randall L. McEntaffer, Drew M. Miles, Thomas J. Peterson, Hannah Marlowe, James H. Tutt, Benjamin D. Donovan, Benedikt Menz, Vadim Burwitz, Gisela Hartner, Ryan Allured, Randall K. Smith, Ramses Günther, Alex Yanson, Giuseppe Vacanti, Marcelo Ackermann, "Line spread functions of blazed off-plane gratings operated in the Littrow mounting," *J. Astron. Telesc. Instrum. Syst.* 2(2), 025001 (2016), doi: 10.1117/1.JATIS.2.2.025001.

Line spread functions of blazed off-plane gratings operated in the Littrow mounting

Casey T. DeRoo,^{a,*} Randall L. McEntaffer,^a Drew M. Miles,^a Thomas J. Peterson,^a Hannah Marlowe,^a James H. Tutt,^a Benjamin D. Donovan,^a Benedikt Menz,^b Vadim Burwitz,^b Gisela Hartner,^b Ryan Allured,^c Randall K. Smith,^c Ramses Günther,^d Alex Yanson,^d Giuseppe Vacanti,^d and Marcelo Ackermann^e

^aUniversity of Iowa, Department of Physics & Astronomy, 210 Van Allen Hall, Iowa City, Iowa 52242, United States

^bMPI für extraterrestrische Physik, Giessenbachstrasse 1, D-85748 Garching, Germany

^cHarvard-Smithsonian Center for Astrophysics, 60 Garden Street, Cambridge, Massachusetts 02138, United States

^dCosine Science & Computing BV, J.H. Oortweg 19, 2333 CH Leiden, The Netherlands

^eCosine Research BV, J.H. Oortweg 19, 2333 CH Leiden, The Netherlands

Abstract. Future soft x-ray (10 to 50 Å) spectroscopy missions require higher effective areas and resolutions to perform critical science that cannot be done by instruments on current missions. An x-ray grating spectrometer employing off-plane reflection gratings would be capable of meeting these performance criteria. Off-plane gratings with blazed groove facets operating in the Littrow mounting can be used to achieve excellent throughput into orders achieving high resolutions. We have fabricated two off-plane gratings with blazed groove profiles via a technique that uses commonly available microfabrication processes, is easily scaled for mass production, and yields gratings customized for a given mission architecture. Both fabricated gratings were tested in the Littrow mounting at the Max Planck Institute for Extraterrestrial Physics (MPE) PANTER x-ray test facility to assess their performance. The line spread functions of diffracted orders were measured, and a maximum resolution of 800 ± 20 is reported. In addition, we also observe evidence of a blaze effect from measurements of relative efficiencies of the diffracted orders. © The Authors. Published by SPIE under a Creative Commons Attribution 3.0 Unported License. Distribution or reproduction of this work in whole or in part requires full attribution of the original publication, including its DOI. [DOI: [10.1117/1.JATIS.2.2.025001](https://doi.org/10.1117/1.JATIS.2.2.025001)]

Keywords: x-ray spectroscopy; off-plane gratings; x-ray diffraction; grating fabrication.

Paper 15061 received Jul. 12, 2015; accepted for publication Mar. 14, 2016; published online Apr. 25, 2016.

1 Introduction

Soft x-ray wavelengths (10 to 50 Å) are host to a number of transition lines helpful in characterizing astrophysical plasmas in energetic environments. Grating spectrometers are the instrument of choice for observing spectra in this bandpass and typically consist of three major components: a set of focusing optics, a grating array, and a detector array. The focusing optic collects light from the source and directs it toward a focus several meters down the optical axis. Instead of being allowed to reach the focus, however, the converging light is intercepted by an array of grating elements. The periodic structure present on the gratings diffracts the converging light based on wavelength. The diffraction pattern is then imaged with an array of detectors at the focal plane, and the source spectrum is reconstructed based on the observed diffraction pattern.

Grating spectrometers are employed on currently operating missions like the Chandra X-ray Observatory and XMM-Newton. However, the science requirements of future x-ray spectrometers necessitate significant improvements in instrument performance. Arcus, for example, is a proposed x-ray grating spectrometer to be mounted on the International Space Station requiring resolution of $R(\lambda/\Delta\lambda) > 2000$ and an effective area of $>400 \text{ cm}^2$ over 21.6 to 25 Å bandpass in order to perform its critical science.¹ This represents a substantial

improvement in both metrics over currently existing capabilities and will require significant investment in enabling technologies.

Off-plane reflection gratings are one such enabling technology, offering the ability to work at high dispersion while maintaining excellent throughput. In the off-plane mount (Fig. 1), the grating grooves are oriented quasiparallel to the direction of the incoming light. This geometry yields a diffraction pattern in which the outgoing orders are constrained to the surface of a half-cone, and hence is often referred to as conical diffraction. The grating equation for the off-plane mount is

$$\sin \alpha + \sin \beta = \frac{n\lambda}{d \sin \gamma}, \quad (1)$$

where d is the groove period, λ is the wavelength of the diffracted light, n is the order number, γ is the half-cone opening angle between the incident beam and the groove direction, α is the azimuthal angle between the reflected (zeroth-order) spot and the grating normal as projected into the grating focal plane, and β is the azimuthal angle between the diffracted spot and the grating normal projected into the grating focal plane. In this paper, we use a prime (') to denote the coordinate system defined by the grating, and define the grating focal plane to be the plane that is perpendicular to the direction of the central grating groove (z') and contains both the telescope focus and the zeroth-order reflection.

*Address all correspondence to: Casey T. DeRoo, E-mail: casey-deroo@uiowa.edu

While constrained to lie on the half-cone, the spectral information is contained in only one dimension, as can be shown by differentiating Eq. (1) with respect to the dispersion direction $x' (= L \sin \gamma \sin \beta)$.

$$\frac{d\lambda}{dx'} = \frac{10^7 \text{ \AA}}{nLD \text{ mm}}. \quad (2)$$

Here, D is the groove density ($\equiv 1/d$) and L is often referred to as the throw, which sets the size scale of the system. Thus, by Eq. (2), the spectral width of a line is measured by its physical extent in the dispersion direction, and the resolution of a spectrometer is governed by the width of the diffracted spot.

Akin to in-plane reflection gratings, off-plane gratings can be blazed to achieve maximum diffraction efficiency at a given wavelength. This geometric effect is brought about under a specific mounting condition, known as the Generalized Maréchal and Stroke mounting² or the off-plane Littrow mounting. The off-plane Littrow mounting is realized when $\alpha = \beta = \delta$, where δ is the facet angle of the grating. In this mounting, off-plane gratings are theoretically capable of achieving diffraction efficiencies approaching the reflectivity of the grating material.³

In this paper, we present first results from two blazed off-plane reflection gratings made via a fabrication method capable of producing high-performance flight gratings. The fabricated gratings were tested at the MPE PANTER x-ray test facility. A silicon pore optics (SPO) stack was used in conjunction with the gratings to form a spectroscopic system, and the line spread functions (LSFs) of the diffracted orders were measured in order to assess grating performance. The fabrication requirements of high-performance off-plane gratings are explained in Sec. 2.1 and the manufacturing method used for the gratings tested here is described in Sec. 2.2. An overview of the experimental setup is given in Sec. 3, the details of placing the grating into the Littrow mounting in Sec. 4.1, and a walkthrough of the data reduction process in Sec. 4.2. A discussion of the results of the test campaign is presented in Sec. 5. The significance of the

work performed here, as well as a brief outline of the work to be performed in the future, is discussed in Sec. 6.

2 Off-Plane Grating Fabrication

2.1 Fabrication Requirements

Meeting the performance specifications of future spectrometers like Arcus requires a high-performance diffraction grating, i.e., a grating capable of 40 to 60% throughput while operating at $R > 2000$. To achieve optimal resolution and throughput, off-plane gratings require a customized facet and ruling geometry. First, the grating grooves must be radially ruled in order to realize high resolution.⁴ This radial fanning of the grooves matches the convergence of the incident beam and ensures the inherent point spread function (PSF) of the telescope is not aberrated. The facets of the grating grooves must also be specially shaped to realize the off-plane blaze condition. A grating with a triangular groove profile placed in the Littrow mounting realizes high diffraction efficiencies for a segment of the diffraction arc near the direction of the facet normal [see Fig. 1(b)]. This segment is equivalent to a range of wavelengths for a given order. Hence, by tuning the facet angle during manufacture, the blaze effect can be used to increase a spectrometer's effective area near particular lines of interest.

In order to diffract at x-ray wavelengths, the groove densities for off-plane gratings must be large compared to in-plane diffraction gratings. Typical groove densities for off-plane gratings range from 4000 to 10,000 grooves/mm. The groove pattern must be producible over large formats ($\sim 100 \text{ cm}^2$) in order to achieve adequate geometric throughput at grazing incidence. Finally, the manufactured gratings need to meet the figure requirements for the spectrometer in question. Any grating substrate deviations from flat translate into local variations of grating orientation. These local variations blur the LSF at the focal plane and compromise overall instrument performance. Grating figure tolerances can be derived by considering the effect of grating misalignments on instrument performance.⁵ In sum, the gratings for a high-performance spectrometer should have (1) radially fanned grating grooves, (2) blazed facets,

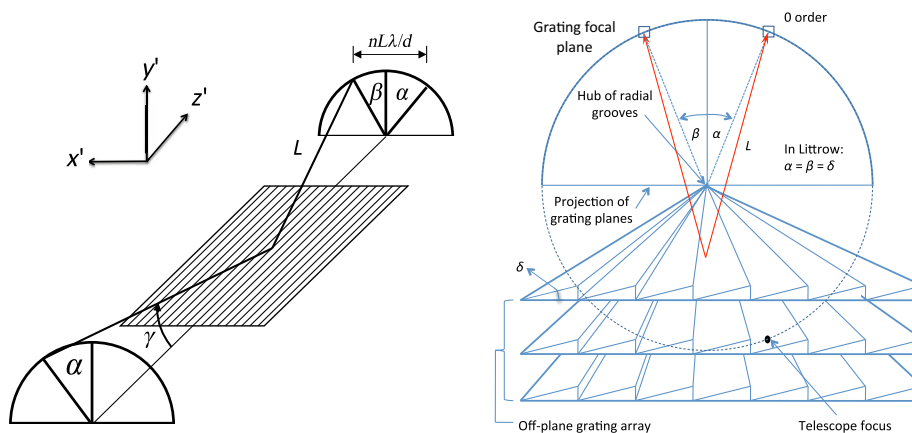


Fig. 1 The diffraction geometry of off-plane gratings. (a) Light incident on the grating is parameterized via the half-cone angle γ and a rotation angle α about the groove direction z' . Diffracted light is constrained to the surface of a cone of the same half-cone angle γ , forming the arc of diffraction. (b) As seen in projection, light that would converge to the telescope focus is instead incident on an array of off-plane gratings. This light is then reflected to the α or diffracted to an angle β . This grating is operated in the Littrow mounting, where the $\alpha = \beta = \delta$, the facet angle.

(3) high groove densities, (4) large patterned areas, and (5) optical figure quality.

2.2 Fabrication Procedure

Off-plane gratings meeting all of these requirements can be manufactured via a microfabrication process outlined in Fig. 2. The fabrication procedure outlined here builds on the work first performed by Franke et al.,⁶ who manufactured an x-ray reflection grating using an anisotropic potassium hydroxide (KOH) etch to form blazed facets in a silicon substrate. A further iteration of blazed x-ray reflection grating fabrication was performed by Chang et al.⁷ and Chang et al.,⁸ who employed ultraviolet nanoimprint lithography (UV-NIL) to replicate a blazed silicon master also produced using the KOH etch technique. However, both of these authors employ interference lithography to create gratings that are straight ruled, rather than the radial rule required for high performance in the off-plane mounting.

The grating fabrication process outlined in the present work uses electron beam lithography (EBL) and deep UV (DUV) projection lithography to produce a radially ruled grating premaster.⁹ The resulting premaster then serves as the mold in a thermal NIL patterning step, creating a radially ruled etch mask for a subsequent KOH etch step. Thus, the technique presented here builds on these previous works, combining the flexibility of patterning with EBL and DUV projection lithography, the anisotropy of KOH etch technique, and the ease of replication offered by UV-NIL to produce radially ruled, blazed x-ray reflection gratings that can be made in large numbers.

We also demonstrate the use of silicon wafers with crystallographic orientations besides $\langle 111 \rangle$ and $\langle 100 \rangle$ in order to manufacture gratings with facet angles near those proposed for off-plane x-ray spectrographs. In grating fabrication processes with a KOH etch step, the blaze angle of the grating is set by the angle between the $\langle 111 \rangle$ direction and the wafer normal. The grating grooves are then patterned parallel to the $\langle 01\bar{1} \rangle$ direction

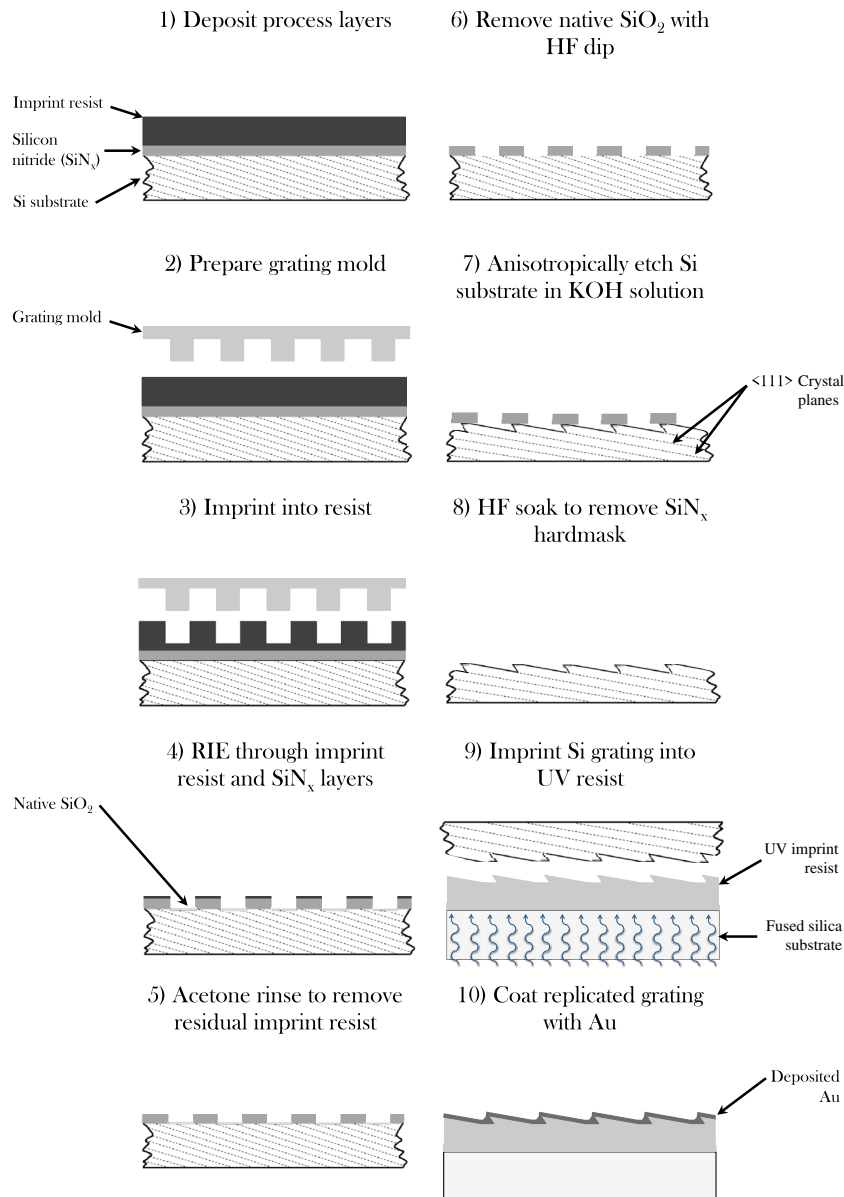


Fig. 2 Procedure for fabricating off-plane gratings.

Table 1 Facet angles achievable using different crystallographic orientations of silicon wafers.

Wafer orientation	Blaze angle (deg)
$\langle 111 \rangle$	0 deg
$\langle 211 \rangle$	22.4 deg
$\langle 311 \rangle$	29.5 deg
$\langle 511 \rangle$	38.9 deg
$\langle 711 \rangle$	43.3 deg
$\langle 100 \rangle$	54.7 deg

in order to bound the KOH etch by $\{111\}$ planes. Franke et al.⁶ and Chang et al.⁸ set the facet angle of their fabricated gratings by dicing a $\langle 111 \rangle$ ingot off-axis, while Chang et al.⁷ used both $\langle 100 \rangle$ and off-axis cut $\langle 111 \rangle$ Si wafers. However, silicon foundries are typically only capable of realizing off-axis cuts of <10 deg, well below the blaze angles proposed for notional off-plane x-ray spectrographs. By way of an example, Arcus requires a blaze angle near 30 deg, while the Off-plane Grating Rocket Experiment (OGRE) proposes to use gratings with a 28 deg blaze.¹⁰ By using other commercially available crystallographic orientations of silicon, however, a variety of blaze angles can be obtained. The resulting facet angles for a number of common silicon wafer crystallographic orientations are given in Table 1. Furthermore, through off-axis cutting of wafers with different crystallographic orientations, it is possible to obtain any blaze angle that might be desired for an off-plane grating spectrometer in the future.

In the interest of completeness, the specifics of the fabrication process employed are detailed here. First, a silicon wafer of the desired orientation is coated with two process layers: a 30 nm layer of silicon nitride (SiN_x) deposited via low-pressure chemical vapor deposition and a 95-nm-thick layer of NXR-1025 nanoimprint resist deposited via spin coater (Fig. 2, step #1). These layers are deposited over the thin native silicon dioxide layer present on the substrate. Next, a grating premaster with the desired groove distribution is obtained and prepared for use (step #2). The premaster is a grating that has the desired groove density and radial convergence, is identical in size to the final flight gratings, and will serve as a mold for the nanoimprint process. However, the premaster has a laminar (i.e., square wave) groove profile and lacks the figure quality required for flight gratings. Prior to use, the premaster is coated with a mold release agent to aid in separation of the mold from the substrate after imprinting. The premaster is then aligned to a foundry-provided wafer flat indicating the $[01\bar{1}]$ direction and the grating pattern imprinted into the resist using a Nanonex NX-1006 nanoimprint tool (step #3). Any nanoimprint resist remaining in the groove troughs is then etched with a reactive ion etch in Ar/O_2 plasma performed at 10 mTorr and 40 W RF, and the SiN_x layer etched in an O_2/CHF_3 plasma at 100 mTorr and 150 W RF (step #4). A rinse step (step #5) in acetone removes any remaining nanoimprint resist, leaving a silicon nitride hardmask matching the grating mold pattern in negative. A dip in buffered hydrofluoric acid (HF) (step #6) removes the native layer of silicon dioxide, exposing bare silicon between strips of the nitride hardmask. The sample is then transferred

to a chemical bath for an anisotropic KOH wet etch (step #7) to sculpt the triangular shape of the groove facets. After terminating the KOH etch with a brief soak in deionized water, the silicon nitride mask is removed by a soak in HF (step #8).

At this point, the only requirement listed in Sec. 2.1 not met by the existent sample is optical figure quality. Silicon wafers have global flatness specifications that are outside the figure qualities needed for off-plane gratings.⁵ Fused silica substrates, on the other hand, can be manufactured to be optically flat to high precision at reasonable cost. By imprinting the blazed silicon grating into resist on a fused silica substrate (step #9), the radially ruled, blazed grating profile can be replicated on a surface meeting the required figure. UV-NIL is employed for this final replication step. As a secondary benefit, a second imprint makes the production of flight gratings a more cost- and time-efficient process, as the same silicon grating can be used for multiple imprints, boosting process yield. The deposition of a thin, x-ray reflective layer over the fabricated grating (step #10) then yields an off-plane grating meeting all the fabrication requirements described in Sec. 2.1.

3 PANTER Test Assembly

Two gratings with different facet angles were fabricated using the anisotropic KOH wet etch method described in Sec. 2.2 and tested at the PANTER x-ray test facility.¹¹ The PANTER facility consists of several x-ray sources housed at one end of a 120-m-long, 1-m-diameter vacuum chamber. This forms a long beamline, limiting the angles of divergence from the x-ray source and resulting in a quasicollimated beam. At the opposite end, a 12-m-long, 3.5-m-diameter instrument chamber is joined to the beamline and houses several customizable optical benches, which can be maneuvered with vacuum stages.

The off-plane grating test assembly employed at the PANTER facility for this set of tests consisted of an SPO stack that serves as a focusing optic, an off-plane grating mechanical interface affixed to an optical bench capable of changing the mounting of a grating *in situ*, and a suite of x-ray detectors to sample the diffraction pattern at the focal plane. A diagram showing the relative positions of the components is shown in Fig. 3. An electron impact source with an Mg target and a 12.5- μm -thick filter was used to generate the x-ray flux. The Mg $K\alpha$ line is composed of two primary components, Mg $K\alpha_1$ and Mg $K\alpha_2$, separated by 0.265 eV at a 2:1 intensity ratio.¹² For the purposes of this paper, we refer to these lines together as the Mg $K\alpha$ line with a central wavelength of 9.8900 Å.¹³

3.1 Silicon Pore Optics

SPO¹⁴ have been developed for the past 10 years by a consortium led by Cosine Research and have become the main technology for the x-ray mirrors of the Athena mission.¹⁵ SPO are formed from highly polished silicon wafers, which are diced into a rectangular shape and ribbed, leaving a thin membrane on one side used to reflect the x-rays and a number of ribs on the opposite side that are used to bond to the next plate. A series of plates are then bent and stacked to form pores, which permit x-rays to reflect and pass through the focal plane. By elastically deforming the plates around a conical mandrel and wedging each plate to give a small angular offset matching the change in radial position, the mirror plates can be bent into a conical approximation of paraboloids or hyperboloids, thus enabling the construction of a stiff, lightweight, high-resolution imaging system.

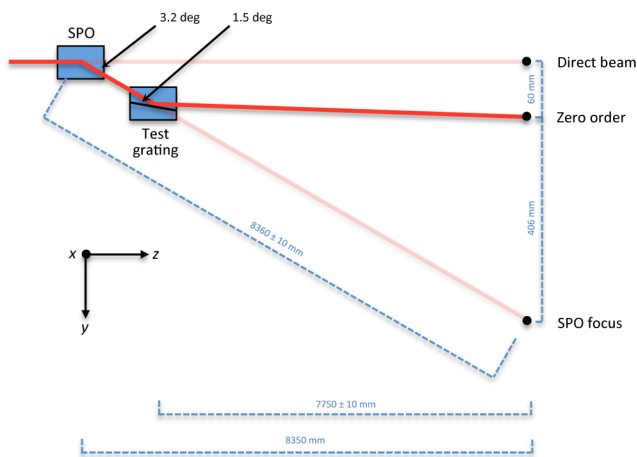


Fig. 3 A diagram showing the optical configuration of the off-plane grating test setup at PANTER. The coordinates specified here (x , y , and z) are system coordinates and are aligned to the grating coordinate system given in Fig. 1 with mechanical tolerances. Distances with quoted errors were directly measured using a laser distance meter, while distances without errors are inferred from the SPO incidence angle and grating graze angle η .

For this campaign, a single SPO stack was built. The geometry of the stack approximates the geometry of a parabolic reflector. The stack consists of 13 plates with radii between 439 and 450 mm, width of 66 mm, and axial length of 22 mm. The constructed SPO realize its best focus at an axial distance of 8350 ± 10 mm and is constructed such that the incidence angle for on-axis measurements is 1.6 deg.

In terms of mirror geometry, the constructed SPO stack is similar to the primary SPO stack for the proposed Arcus mission. However, due to time and budget constraints, the methods employed to build this particular stack are atypical of SPO production. First, this stack was shaped on a simple aluminum mandrel rather than one of high-quality polished silicon. In addition, the stacking device employed to deform the plates around the mandrel was not retooled to accommodate the change in radii from the nominal SPO stacking radius of 800 mm. Thus, the performance of the SPO module used in these tests is not representative of the state-of-the-art in SPO manufacture. An image of the SPO stack prior to installation in the chamber is shown in Fig. 4.

A series of aperture masks mounted to vacuum stages was used to control the illumination of the SPO by the source. For the present test of blazed gratings, a single mask measuring 42 mm by 11 mm was positioned in front of the SPO, subaperturing the optic to this width and radial extent, respectively. This mask represents an effective SPO illumination percentage of 63% and will hence be referred to as the 63% mask. However, during initial characterization of the optic, a mask measuring 6 mm by 11 mm (representing an effective illumination percentage of 9%, and hence dubbed the 9% mask) was also employed to initially characterize the SPO.

3.2 Detectors

Three focal plane instruments were employed to sample the SPO focus and the arc of diffraction. The Position Sensitive Proportional Counter (PSPC) is a gas-proportional counter and is the flight spare of detector onboard ROSAT.¹⁶ Though the PSPC has relatively low spatial resolution, the large format

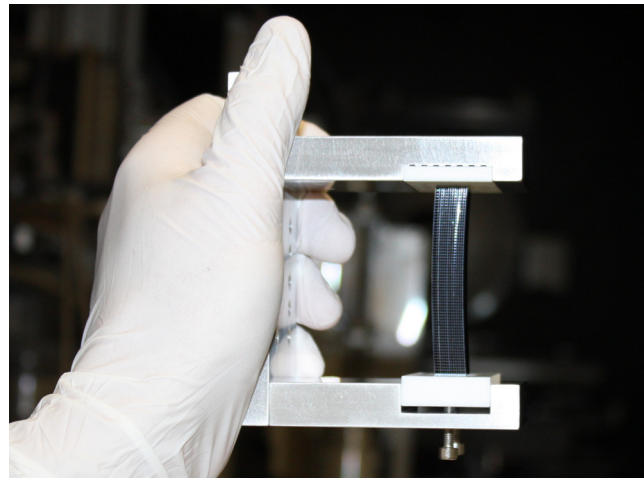


Fig. 4 An image of the SPO stack before being installed in the PANTER x-ray test chamber.

of the detector ($\varnothing = 80$ mm) is useful for viewing large portions of the arc of diffraction at once and establishing rough alignment. A CCD camera is then used to image diffracted orders with higher spatial resolution. The Third Roentgen Photon Imaging Camera (TRoPIC) is a back-illuminated CCD and is a smaller version of the detector baselined for the eROSITA mission.¹⁷ The second CCD camera in use is the Princeton Instruments X-ray Imager (PIXI), a soft x-ray imager with a pixel size of $20 \mu\text{m}$. PSPC and TRoPIC were mounted just above the nominal horizontal (y in Fig. 3) system axis, while PIXI was mounted just below. The suite of detectors is capable of ± 250 mm of motion along the optical axis (z in Fig. 3) and has enough travel to cover the entire grating focal plane in the y direction and a total of 150 mm in the x direction. At the nominal grating graze angle of 1.5 deg, the arc of diffraction is too large to be fully sampled in the dispersion direction, thus some diffracted orders were not accessible to any detector. The nominal position of the detectors was chosen to allow TRoPIC to sample the SPO focus, the reflected beam (zeroth order), some positive orders, and limited negative orders, and to allow PIXI to sample the SPO focus (see Figs. 5 and 6).

3.3 Gratings

Both fabricated gratings tested at PANTER were patterned using a premaster identical to the gratings tested in Ref. 9, which have a nominal groove density of 6033 gr/mm, a radial convergence matching an 8.4 m focal length telescope, and a format measuring $25 \text{ mm} \times 32 \text{ mm}$, where the long edge is parallel to the ruling direction. The first grating (for ease of reference, Grating 1) was made using a $\langle 111 \rangle$ silicon wafer, which was cut 10 deg off-axis, forming a 10 deg angled facet. This profile was successfully transferred to a 4 in. fused silica wafer and coated with a 10-nm-thick layer of gold. The second grating was made using a $\langle 311 \rangle$ silicon wafer (Grating 2), yielding a 29.5 deg facet angle, similar to the facet angles required for several future spectrometers including Arcus and OGRE.¹⁰ Due to time and budget constraints, the blazed silicon grating was tested directly rather than transferring the grating pattern to a fused silica wafer, and was cleaved to measure approximately 35 mm by 45 mm (where the long edge is again parallel to the ruling direction) for mounting purposes.

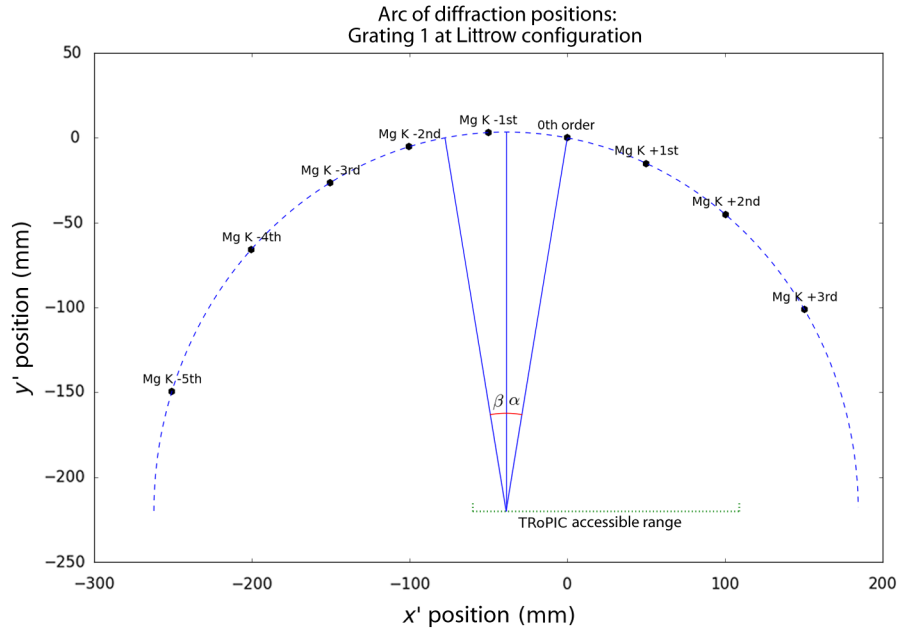


Fig. 5 A nomogram of the diffraction arc for Grating 1 in the Littrow mounting described. As the grating has a facet angle of $\delta = 10$ deg, placing the grating in the Littrow mount means that $\alpha = \beta = 10$ deg.

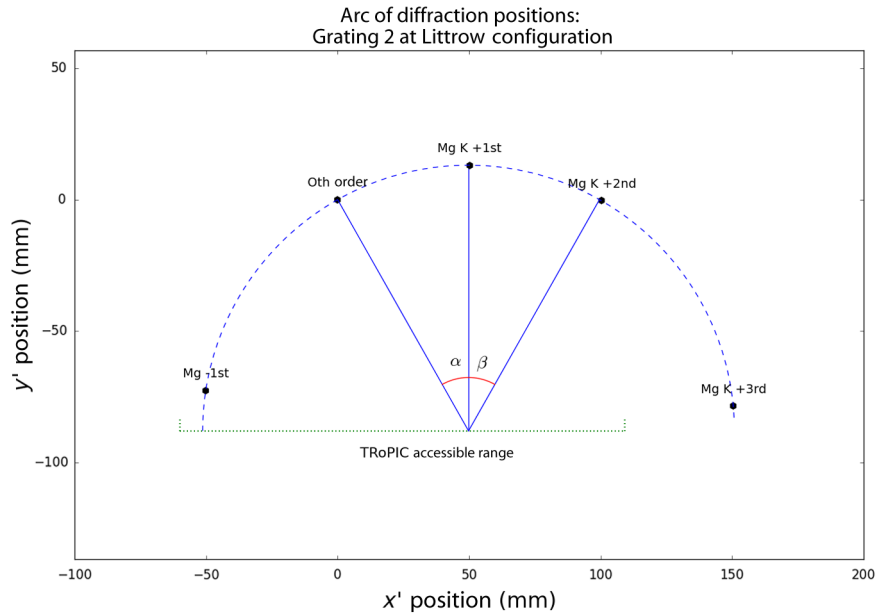


Fig. 6 A nomogram of the diffraction arc for Grating 2 in the Littrow mounting described. In the Littrow mounting, $\alpha = \beta = \delta$, and the facet angle $\delta = 29.5$ deg for Grating 2.

These gratings were mounted on a vacuum stage stack with four degrees of freedom: linear motion in the cross-dispersion direction y , linear motion in the dispersion direction x , grating graze angle η (rotation about x), and grating yaw Ψ (rotation about y). The grating testing positions were found prior to evacuating the chamber via the use of an optical laser mounted at the source end of the beamline. The laser spot could be passed through the SPO, and each grating maneuvered via vacuum stages until illuminated by the focused beam. The nominal grating graze angle of 1.5 deg was set by measuring the distance between the reflected spot and the direct SPO focus as created by this same optical laser, and has an accuracy of 4 arc min given

the uncertainty in the measured distance between the SPO stack and the detector plane (± 10 mm over 8360 mm). Finding the zero yaw position of each grating was performed under x-ray illumination. Deviations from zero yaw move the groove hub, or point at which the radial grooves converge, increasing the radius of the diffraction arc without changing the zero-order position. A yaw misalignment thus causes positive and negative orders to appear at different cross-dispersion coordinates relative to zeroth order. To perform the initial yaw alignment, PSPC was employed to examine large sections of the diffraction arc until positive and negative orders were symmetrically distributed about the zeroth order. TRoPIC measurements were then used to

perform a fine yaw alignment by centroiding ± 1 st Mg K α orders and adjusting the grating yaw until both orders were measured to be at the same cross-dispersion pixel value. Changes in centroid height were easily distinguishable with yaw rotation step sizes of 1.5 arc min. We, therefore, estimate the accuracy of this method of yaw alignment to be 0.75 arc min.

4 Measurements

4.1 Test Configurations

Following the characterization of each grating's orientation with respect to the stage axes, each grating was then placed in the Littrow mounting. Functionally, reaching the Littrow mount involves setting the graze angle η and grating yaw Ψ around the fixed geometry of the beamline and SPO: increasing the graze angle serves to increase the length of the chord between the SPO focus and zero order, while increasing the yaw of the grating increases both the radius of the diffraction arc and α in the grating equation. Recall that in the Littrow configuration, $\alpha = \beta = \delta$. Thus, the blaze wavelength λ_b for a given order n is the wavelength diffracted to an angle $\beta = \delta$ and is given by the expression

$$\lambda_b = \frac{2d \sin \gamma \sin \delta}{n}, \quad (3)$$

which can be derived from Eq. (1). The graze angle of the grating can thus be chosen to place an Mg K α order at the blaze wavelength. Once the graze angle is set, the grating is then placed into the Littrow mounting by yawing the grating until the following relationship is satisfied:

$$\sin \Psi = \tan \eta \tan \delta. \quad (4)$$

This relationship describing the Littrow mount is independent of the length scale of the system and can be derived from geometrical considerations.

Figure 5 shows the diffraction geometry of the test configuration for Grating 1. The groove facets of Grating 1 were blazed toward negative orders. A graze angle of $\eta = 1.5$ deg was chosen to be identical to the graze angle for Arcus and OGRE. However, the blaze position does not correspond to the wavelength of any line fluoresced by the Mg target, lying approximately halfway between Mg K α -2 nd order and Mg K α -1 st order. For measurements of Grating 1, TRoPIC was used to image the Mg K α -1 st and $+1$ st order lines, as well as the zeroth-order reflection.

The facet angle of $\delta = 29.5$ deg defines a different diffraction geometry for Grating 2 when placed in the Littrow mounting, which is shown in Fig. 6. The groove facets of Grating 2 were blazed toward positive orders. Testing Grating 2 at a graze angle of $\eta = 1.5$ deg was precluded by the extent of detector travel: accessing the location of the ideal β at such a graze angle required 250 mm of stage travel in the dispersion direction

relative to zeroth order, which exceeds the maximum travel extent range of 150 mm as discussed in Sec. 3.2. Instead, a graze angle of 0.6 deg was selected for testing this grating, which places the Mg K α $+2$ nd order line near the location of highest diffraction efficiency. For Grating 2, the Mg K α 0th, -1 st, $+1$ st, and $+2$ nd diffraction orders were measured.

The physical size of each grating relative to the aperture of the SPO means that each grating undersamples the PSF produced by the optic, even with the 63% mask in place. As seen in projection, Grating 1 represents an effective aperture 25 mm in width and 0.84 mm in radial extent (a 3% effective illumination), while the Grating 2 subapertures the SPO to 25 mm by 0.33 mm (a 1% effective illumination). As no attempt was made to align the gratings to an individual SPO plate, Grating 1 thus likely samples around two SPO reflectors, while Grating 2 samples a single reflector. A summary of each grating's characteristics and mounting is provided in Table 2.

4.2 Data Reduction

As implied by Eq. (2), the spectral information of a diffracted order is contained only in x' , the dispersion direction. Hence, the LSF is measured by collapsing the image in the cross-dispersion direction and measuring the total number of photons in each spatial bin. For measurements taken with TRoPIC, the CCD images are converted from native ADC (analog to digital conversion) units into individual photon events via event processing (photon counting), which is integrated into the onboard electronics. These output an event list characterized by detector coordinates, pulse height, and event time. A set of grading criteria is used to determine good events, and a split pixel analysis is then performed to give photon positions within subpixel accuracy. The resulting good event list is then minimally binned to the effective spatial resolution of 20 μm .¹⁸

PIXI, on the other hand, has no integrated photon counting mode. Data taken with PIXI are reduced by the subtraction of a dark frame, where the dark frame is an array matching the format of the CCD whose values are a pixel-by-pixel average of a series of frames taken at an identical stage position with the x-ray source turned off. This same series is also used to construct an array called a variance frame, in which the array values are the pixel-by-pixel standard deviation σ_{pix} of the series. The variance frame is then used to threshold the dark-corrected images by setting to zero any pixels falling below $3\sigma_{\text{pix}}$. The resulting images are then in units of integrated ADC counts.

Next, a rotation is applied to the data to account for the misalignment of the dispersion direction to the horizontal detector axis. The dispersion direction x' is set by the orientation of the grating and is perpendicular to both the groove direction and the grating normal. While the grating is nominally aligned to the detector axes via mechanical tolerances, the extent of the LSF in the y direction means that a small angular misalignment between the detector axes and grating axes can yield a significant change in the measured width of the line. In order to

Table 2 An overview of the gratings tested at the PANTER x-ray facility, the test configuration for each grating, and the diffraction orders imaged.

Grating	Facet angle δ (deg)	Graze angle η (deg)	Number of SPO plates sampled	λ_b ($n = 1$) (Å)	Mg K α orders imaged
Grating 1	10	1.5	1 to 2	15.3	-1 st, $+1$ st, 0th
Grating 2	29.5	0.6	1	19.7	-1 st, $+1$ st, $+2$ nd, 0th

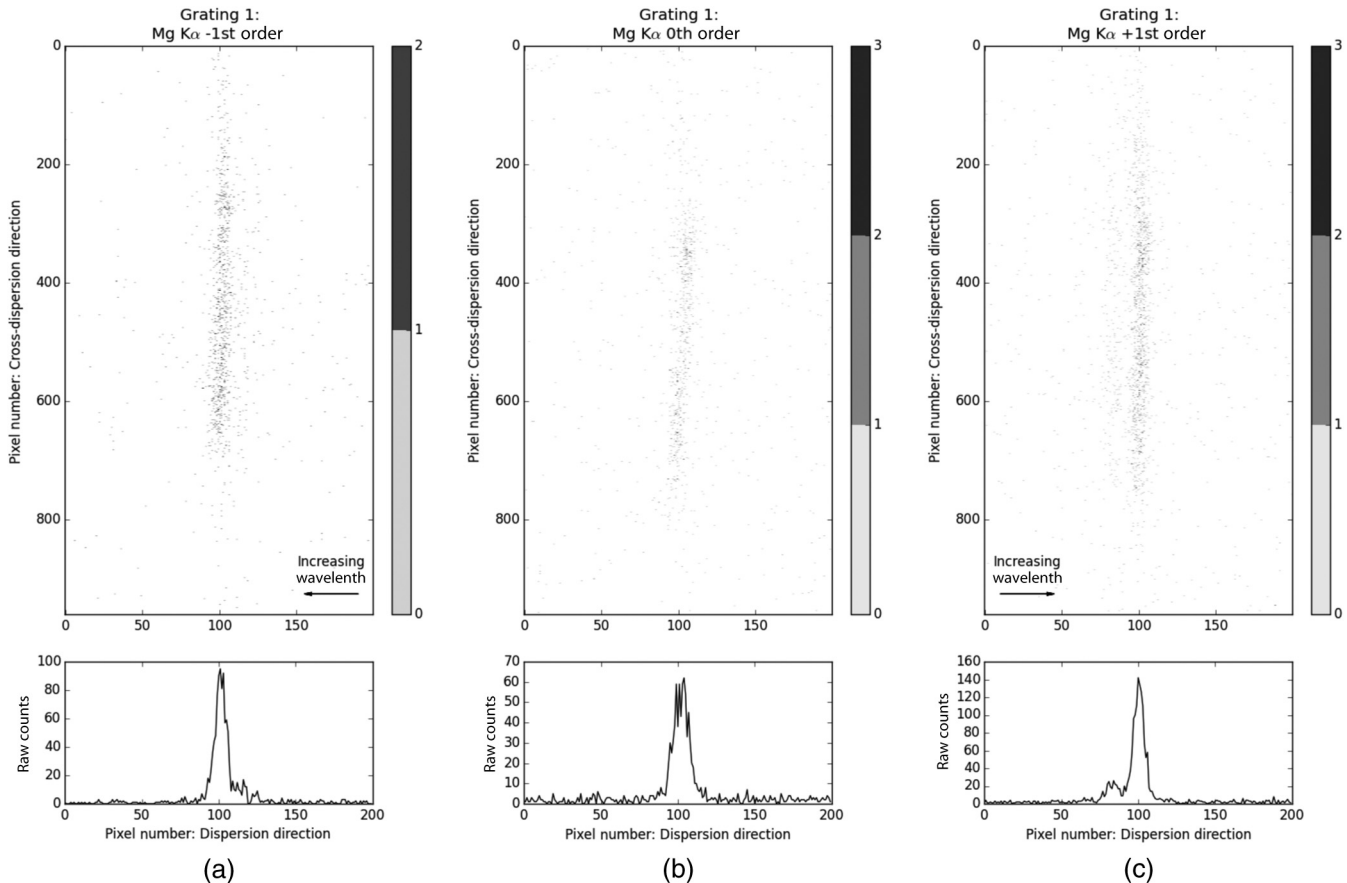


Fig. 7 TROPIC images of (a) Grating 1 -1 st order, (b) Grating 1 0th order, and (c) Grating 1 $+1$ st order lines. The insets below show the data collapsed in the cross-dispersion direction to yield the LSFs. A spectral feature consistent with the $\text{Mg K}\alpha_3$ satellite line (9.823 \AA) is visible to the right of the $\text{Mg K}\alpha$ line in (a) and to the left of the $\text{Mg K}\alpha$ line in (c).

account for this misalignment, the absolute position of each order in system coordinates (x, y) is first measured using the stage location and the LSF centroid as measured on the detector and defining the origin to be the zeroth-order spot. The rotation angle required to convert system coordinates into grating coordinates (x', y') is then derived by enforcing the condition that the x' positions of each diffracted order are appropriate integer multiples of one another, where the integer multiple is given by the known diffraction order. In this way, the order locations in the grating coordinate system are made to be self-consistent with periodic diffraction in x' , e.g., the $+2$ nd-order $\text{Mg K}\alpha$ line is twice as far in x' from zeroth order as the $+1$ st-order $\text{Mg K}\alpha$ line. The derived rotation angles are each found to be <1 deg, which is in keeping with the mechanical alignment tolerances of the detectors to the grating stage stack. These rotations are then applied to the data from each grating to yield CCD images where the horizontal detector axis is aligned to the dispersion direction.

This reduction process yields a set of analysis images that are representative of the spectrometer configuration as tested. The images are subsequently summed in the cross-dispersion direction in order to measure the LSF. By way of an example, Fig. 7 shows cropped analysis images and LSFs of Grating 1 $\text{Mg K}\alpha$ 0th order, $\text{Mg K}\alpha$ $+1$ st order, and $\text{Mg K}\alpha$ -1 st order. Rather than modeling the observed LSFs with an expected functional form and extracting line widths from a model-dependent fit, we characterize each LSF by measuring its half-energy width

(HEW). The HEW provides an unambiguous, model-independent method of quantifying the spatial extent of flux concentrated in an x-ray feature. The HEW is found by constructing the cumulative distribution function of the LSF and calculating the spatial extent needed to enclose 50% of the total number of photon events, N_{tot} . The upper and lower bounds on the HEW are calculated by determining the spatial extent needed to bound enough events to be within a single Poisson error of half of the total counts in a given line. As each sampled line has sufficient counts for the total number of counts over the given integration time to be normally distributed, we expect the Poisson counting error $\sqrt{N_{\text{tot}}}$ to converge to σ , the standard deviation of the distribution of total counts over the given integration time. Hence, we refer to the calculated upper and lower bounds as 1σ bounds. It should be understood, however, that σ is in reference to the number of counts contained in the stated spatial extent and is not an error derived by fitting the observed LSF for the HEW.

5 Results and Discussion

The LSFs of all measured orders, as well as the x extent of the SPO focus with the 63% mask in place, are shown in Fig. 8. The diffracted order LSFs of Grating 1 and Grating 2 are shown as insets in Figs. 8(a) and 8(b), respectively, while the SPO focus is shown individually in Fig. 8(c). A summary of all measured HEWs, the corresponding 1σ bounds, and the resolutions achieved are presented in Table 3. As a gentle reminder to

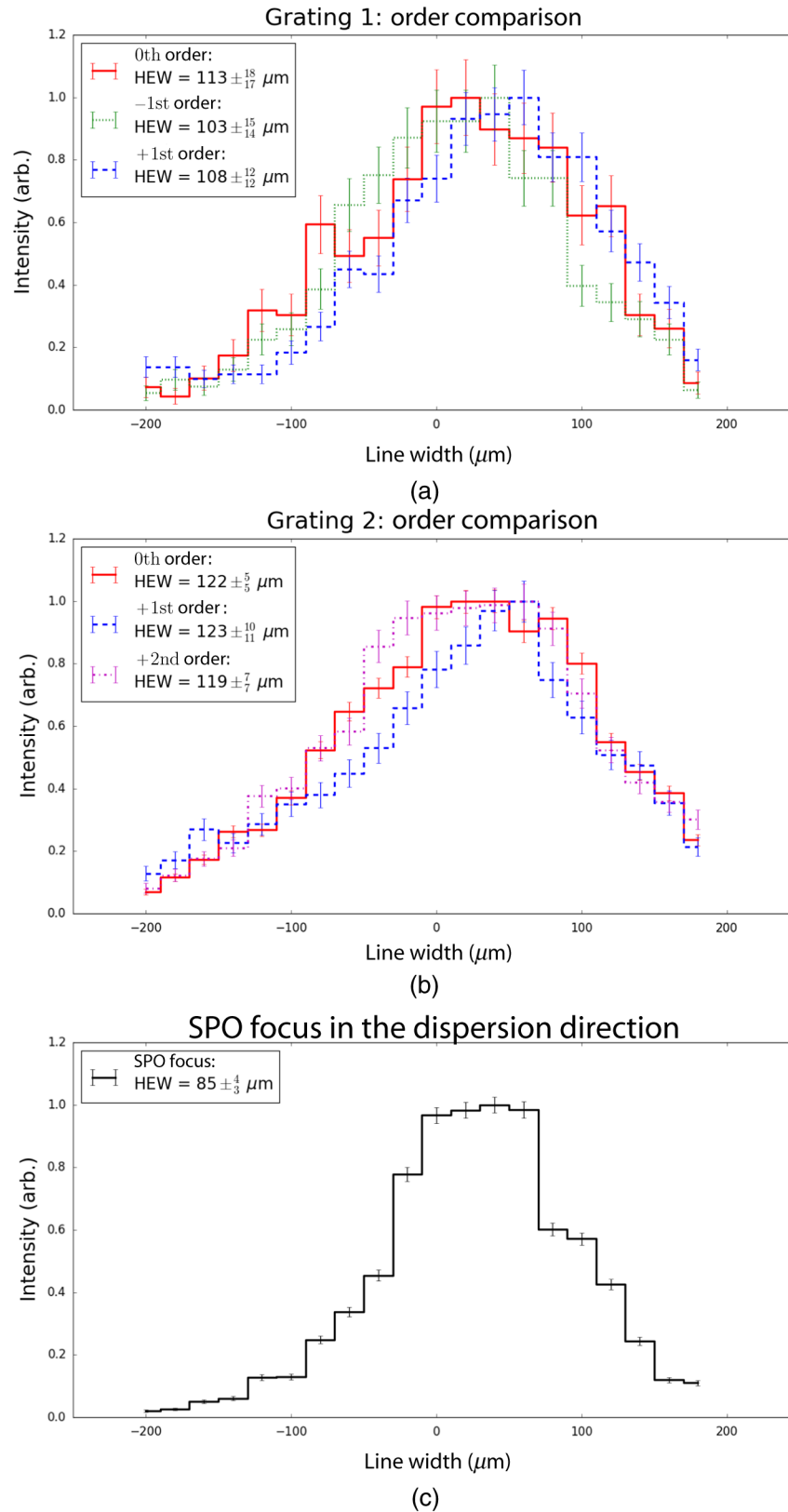


Fig. 8 The LSFs of all observed orders and the PSF of the SPO compared side-by-side. (a) The LSFs of imaged Mg $K\alpha$ orders from Grating 1. Note that because the dispersion direction is reversed from positive to negative orders, any spectral structure in the +1st order Mg $K\alpha$ line should likewise be reversed in the -1st order line. (b) The LSFs of imaged Mg $K\alpha$ orders from Grating 2. (c) The PSF of the SPO focus collapsed in the cross-dispersion direction. Each profile is centered about zero and is normalized to a relative intensity of 1.0.

Table 3 The HEWs of the SPO focus and imaged orders.

Measurements of HEW by diffraction order				
Grating	Order	HEW (μm)	1σ errors (μm)	Est. resolving power ($x/\Delta x$)
Grating 1	0th	113	+18/−17	—
	−1st	103	+15/−14	460 ± 70
	+1st	108	+12/−12	440 ± 50
Grating 2	0th	122	+5/−5	—
	+1st	123	+10/−11	390 ± 30
	+2nd	119	+7/−7	800 ± 20
SPO focus: 63% mask	—	85	+4/−3	—

the reader, Grating 1 and Grating 2 are blazed in opposing directions, have different facet angles, and are tested at different graze angles (see Sec. 4.1 for a detailed summary). Hence, the intensities and LSFs of each measured order should not be expected to be identical from grating to grating. For example, while the Mg K α −1st order was accessible with TRoPIC for both gratings, no concentration of flux was measured at the position of the order for Grating 2. This result is not surprising, given that in the test configuration for Grating 2, the Mg K α −1st order is almost in evanescence and opposite the blaze direction (see Fig. 6). As such, this order is excluded from Fig. 8 and no HEW is reported.

The resolving powers of each grating in the current configuration are estimated by dividing the distance dispersed by the observed HEW and reported in Table 3. In ± 1 st order for both gratings, we find resolving powers near 400 to 450, and we report a maximum resolution of $R = 800 \pm 20$ for Mg K α +2nd order for Grating 2.

5.1 Line Spread Functions of Diffracted Orders

A comparison of the SPO focus, the zeroth-order focus, and diffracted orders can be used to assess whether the LSF of diffracted orders is aberrated due to defects in the fabricated gratings. A broadening of the LSF due to aberration would impact the ultimate resolution of a spectrometer and could complicate the alignment of multiple gratings, reducing the signal-to-noise ratio in observed orders. To accurately compare the measurements of the SPO focus and grating orders, however, a rigorous accounting of possible errors contributing to the observed LSFs must be made.

The base LSF of any diffracted order is the PSF of the focusing element. In the present case, however, the SPO focus as shown in Table 3 is not directly comparable to the LSFs of the diffracted orders as the limited grating size (in comparison to the illuminated SPO area) effectively subapertures the optic. This subaperture would be expected to decrease the width of the PSF. A standard estimate for the reduction in the PSF width for a scatter-dominated x-ray mirror subapertured to an azimuthal range θ employs a $\sin \theta$ scaling law.¹⁹ Applying this scaling law would imply an HEW of $51 \mu\text{m}$ for the SPO PSF illuminating the gratings. However, this $\sin \theta$ scaling law does not

account for the possibility of SPO figure error. Empirical measurements of the SPO focus taken with PIXI during preliminary alignment suggest that the figure error of the optic does make a significant contribution to the width of the SPO focus, and hence, the $\sin \theta$ scaling is not appropriate for the SPO stack used in this test. As mentioned previously in Sec. 3.1, a 9% SPO mask was employed during preliminary alignment of the optic. As employing the 9% mask illuminates a significantly smaller azimuthal extent of the SPO stack, these preliminary alignment data are useful in quantifying the expected subaperture effect from the gratings. The best PSF produced by the SPO during preliminary alignment with the 63% mask (≈ 5.5 deg in azimuth) is measured to have a $135 \mu\text{m}$ HEW. Applying the $\sin \theta$ scaling to the focus achieved with the 63% mask would imply a PSF HEW of $19 \mu\text{m}$ for the 9% mask (≈ 0.8 deg in azimuth), while the best PSF with the 9% mask during this same phase of alignment is measured to have a width of $114 \mu\text{m}$. Thus, we posit that figure error of the SPO plates must also be a contributing factor in the grating-subapertured measurements. Note that as the preliminary alignment data do not have the same focus position used in the test campaign, the SPO PSFs reported here are, therefore, not directly comparable to the grating test data reported in Table 3.

Given the discrepancy between the $\sin \theta$ prediction and the measured SPO focus of the 9% mask during preliminary alignment, we instead estimate the width of the SPO PSF subapertured by the grating during the testing phase by linearly relating the SPO widths measured during preliminary alignment to the azimuthal extents covered by each mask and solving for an azimuthal scale factor S_{az} . This relation is then used to solve for the expected width of the grating-subapertured SPO PSF from the 63% mask data as measured during the test campaign. This method is limited, however, in its ability to account for the radial subaperture of the grating. Each grating is illuminated by 1 to 2 SPO plates, while the mask data represent the integrated contributions of all 13 plates in the SPO stack (albeit over a limited azimuthal range). Thus, this method does not account for plate misalignments and, hence, may overestimate the contribution of the SPO to the observed grating LSFs.

Put mathematically, the scaling method described here calculates the width of the grating-subapertured SPO PSF in the following manner:

$$\begin{aligned} \text{PSFWidth}_{63\% \text{mask,prelim.}} - \text{PSFWidth}_{9\% \text{mask,prelim.}} \\ &= S_{az}(\theta_{63\% \text{mask}} - \theta_{9\% \text{mask}}), \\ \text{PSFWidth}_{\text{grating}} \\ &= \text{PSFWidth}_{63\% \text{mask,test}} - S_{az}(\theta_{63\% \text{mask}} - \theta_{\text{grating}}). \end{aligned}$$

This method yields an estimate of $76 \mu\text{m}$ for the width of the SPO PSF subapertured by both gratings, which we take to be the base width of the LSF for the grating orders.

Next, we compare the zeroth-order LSF to this estimate of the SPO focus to determine whether there is any broadening of the LSF due to grating figure or a mismatch of the sampled focal plane to the geometrically defined grating focal plane. The measured zeroth-order focus of both Grating 1 and Grating 2 is inconsistent with the estimated width of the subapertured SPO focus ($76 \mu\text{m}$). A postanalysis review of the stage positions used during grating measurements shows the diffracted orders of Grating 2 were sampled 2 mm intrafocal of the geometrically defined grating focal plane, while the Grating 1 data were

taken at a distance 6 mm intrafocal of its ideal focal plane. However, a geometric raytrace of the SPO stack demonstrates that for both gratings, the difference in the sampled focal plane and the ideal grating focal plane would not be expected to significantly contribute to the observed width of the zeroth order. The geometric raytrace propagates 10^8 individual rays through a single SPO reflector and grating. Raytrace measurements of the LSF HEW are repeatable at the $1\ \mu\text{m}$ level. Thus, the minimum error distinguishable via the raytrace given the estimated $76\ \mu\text{m}$ HEW of the subapertured SPO is $12\ \mu\text{m}$ rms. Based on the raytrace, the expected rms contribution to the HEW of the zeroth-order spot due to the mismatch of the focal plane is $17\ \mu\text{m}$ for Grating 1 and $<12\ \mu\text{m}$ for Grating 2. This is consistent with axial (z) scans of the SPO focus taken prior to measurements of the gratings, which yield a focus curve predicting an rms contribution of $17\ \mu\text{m}$ for a 6 mm intrafocal sampling and a contribution of $7\ \mu\text{m}$ for a 2 mm intrafocal sampling of the SPO focus.

We, therefore, attribute the observed broadening of the zeroth order to grating-induced figure error. Lacking figure measurements of the gratings within their mounting structure, we instead employ the same geometric raytrace employed in the previous focal plane study but deform the grating surface from flat into a symmetric ellipsoid characterized by a single radius of curvature R_{curv} . This characterization is akin to characterizing the total figure error by a single Zernike polynomial Z_2^0 (defocus) as would be projected onto the format of the grating. The raytraced zeroth-order spot must also be rotated by the measured angle between the narrow dimension of the grating focus and the horizontal detector axis in order to give the width of the aberrated spot in the dispersion direction rather than raytrace system coordinates.

Reproducing the growth of the estimated grating-subapertured HEW ($76\ \mu\text{m}$) to the zeroth-order spot size reported in Table 3 requires Grating 1 to have a radius of curvature of 4.60×10^4 mm, corresponding to a peak-to-valley (P-V) measurement of $2.78\ \mu\text{m}$ over the $32\ \text{mm} \times 25\ \text{mm}$ grating format. This is outside the P-V tolerance specified for the fused silica wafers used for the fabrication of Grating 1, suggesting that the observed figure error may be attributable to stress induced by the grating mount; however, without an interferometric measurement of a fabricated grating on fused silica, figure error native to the grating itself cannot be ruled out. Grating 2 is found to have a smaller radius of curvature, $R_{\text{curv}} = 2.75 \times 10^4$ mm (P-V: $4.65\ \mu\text{m}$ over the grating area). The figure error observed in Grating 2 is not surprising, as the cited flatness specification for the $\langle 311 \rangle$ wafer used in its fabrication is $<40\ \mu\text{m}$ warp over its $76.2\ \text{mm}$ diameter extent, where warp is defined as the sum of the maximum deviations of the wafer above and below the best fit plane.

In addition to quantitatively reproducing the dispersion direction HEWs of the zeroth-order LSFs for both gratings, the results yielded by the raytrace are also qualitatively similar to the images of the LSFs when binned to a pixel scale identical to the TRoPIC detector format. Figure 9 shows side-by-side comparisons of the measured and raytrace-simulated SPO focus and the Grating 1 zeroth-order LSF. As can be seen in Fig. 9, the addition of a symmetric ellipsoidal grating figure error also helps account for the observed growth of the zeroth-order spot in the detector vertical dimension, further supporting the idea that grating figure error is predominantly responsible for the growth of the zeroth-order LSF relative to the estimated PSF of the SPO stack.

We also examine via raytrace whether any growth in the LSFs of diffracted orders is anticipated due to a mismatch of the radial convergence of the gratings. As alluded to in Sec. 2.2, the radial pattern of both fabricated gratings is set by the grating premaster. This premaster is ruled to match a Wolter-I type telescope with an 8400 mm focal length positioned 250 mm behind the intersection point of the paraboloid and hyperboloid. We model both an idealized radial ruling, in which the ruling is perfectly matched to the geometry of the raytrace system, and the ruling of the premaster in our raytrace system and find no discernible change in the LSFs of any of the diffracted orders measured in this paper. Thus, we put an upper bound on the contribution of the mismatch of radial ruling equal to $12\ \mu\text{m}$, the minimum rms contribution to the width of the LSF discernible via raytrace.

Finally, we examine the expected contribution of the finite linewidth of the $\text{Mg K}\alpha$ line on the diffracted LSFs. Citrin et al.²⁰ report an empirically measured full width at half maximum (FWHM) value of 1.10 eV for the $\text{Mg K}\alpha$ x-ray emission line fluoresced with an x-ray tube. From this FWHM value, we calculate the expected HEW assuming a Gaussian distributed line and convert this to a width of $4.99 \times 10^{-3}\ \text{\AA}$ centered around the wavelength of $\text{Mg K}\alpha$. From the empirically observed dispersion of the gratings of $0.208 \pm 0.001\ \text{\AA}/\text{mm}$ in ± 1 st order, this would yield an expected rms broadening of the line by $24\ \mu\text{m}$ in the ± 1 st order and $48\ \mu\text{m}$ in the 2nd order.

Table 4 gives a full summary of the errors characterized in this section and calculates the total expected HEW of each order by adding the expected rms error contributions in quadrature with the anticipated width of the grating-subapertured SPO PSF. In our analysis of the diffracted orders, we have assumed that the $\text{Mg K}\alpha$ line is adequately described as a single Gaussian despite being composed of two closely spaced contributions,¹² and that the effect of the broadening terms can be accurately described as independent errors summed in quadrature. Given these assumptions, we find total expected HEWs are consistent with the measured HEWs for the ± 1 st orders of both gratings, as can be seen by comparing the measured HEWs stated in Table 3 to the expected LSF HEW given in Table 4. However, the total expected width of the HEW for the $+2$ nd $\text{Mg K}\alpha$ line of Grating 2 does not agree with the measurement of this LSF.

We posit that this discrepancy in the width of the $+2$ nd-order $\text{Mg K}\alpha$ line for Grating 2 arises from the poorly understood contribution of the unpatterned substrate surrounding the grating to the zeroth order. We are confident in our effort to understand the SPO focus as subapertured by the format of the patterned grating, which forms the base of the LSF for diffracted orders. However, the unpatterned area surrounding the grating would be expected to contribute to zeroth order in reflection, effectively creating a different subaperture defined by the overlap of the SPO beam and grating substrate. Subtracting the contribution of the unpatterned substrate from our reported measurement of the zeroth-order LSF would serve to reduce the measured HEW by as much as $10\ \mu\text{m}$. Quantifying the exact contribution of the unpatterned substrate to the measured zeroth-order LSF is complicated by the effects of the grating figure, which must be a significant contributing factor to the measured zeroth-order HEW but is degenerate with the effects of a larger subaperture. Therefore, the reported HEW measurement for the $\text{Mg K}\alpha$ $+2$ nd-order LSF of Grating 2 may be consistent with the broadening expected from the finite width of the line if the

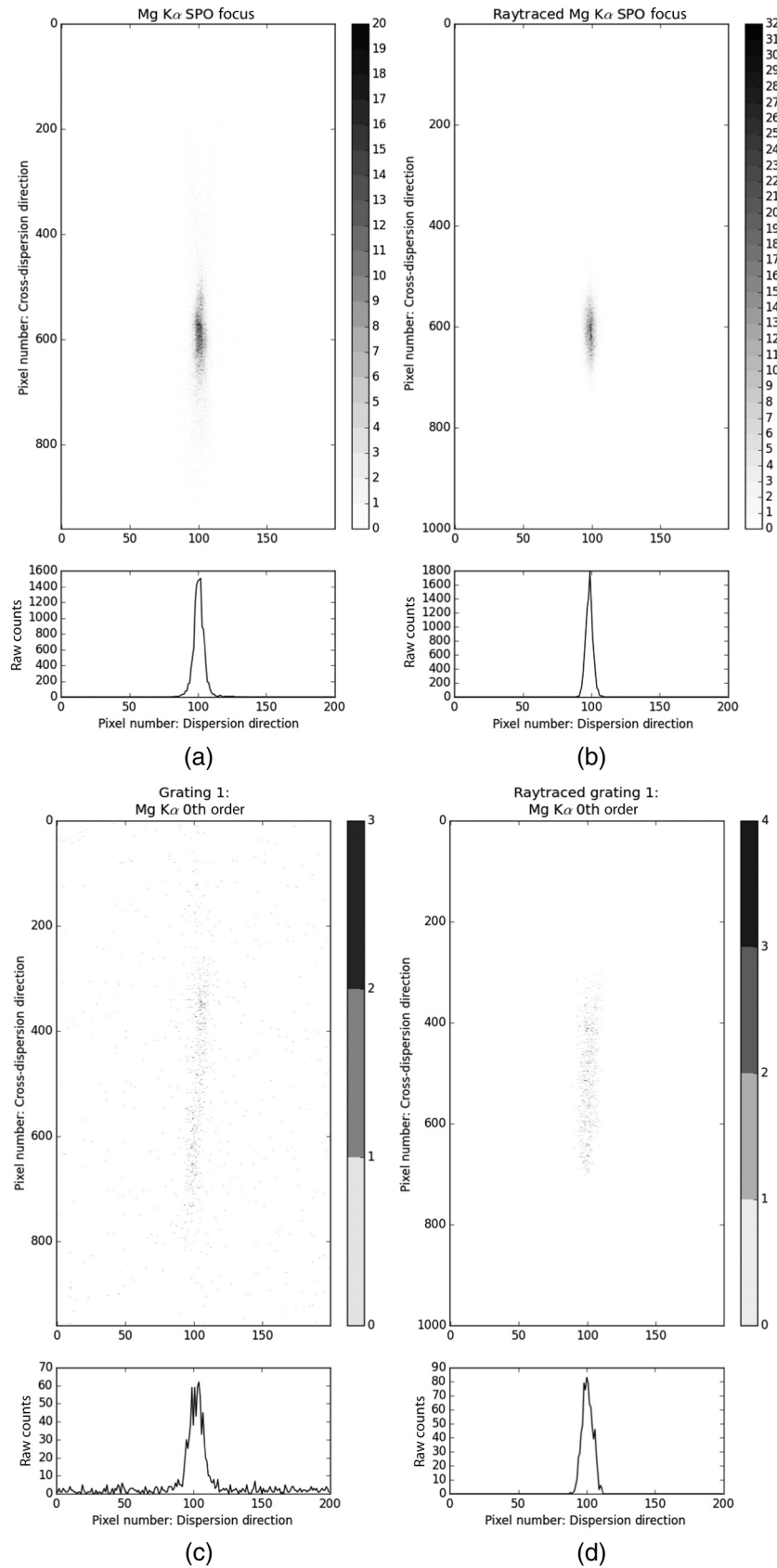


Fig. 9 Measured and raytrace-simulated CCD images of the SPO focus and 0th order focus of Grating 1. Each pixel is $20 \mu\text{m}$ and the images have been summed in the vertical detector dimension to give a line profile. (a) The measured SPO focus with the 63% aperture mask. (b) The raytraced SPO focus with a simulated 63% aperture mask. (c) The measured Grating 1 0th order line. (d) The raytraced Grating 1 0th order line with ellipsoidal figure error ($R_{\text{curv}} = 4.60 \times 10^4 \text{ mm}$).

Table 4 The expected contributions of measurement errors to LSFs of the gratings.

Grating	Errors contributing to the LSFs of diffracted orders					
	Grating 1			Grating 2		
Order	0th order	+1st order	−1st order	0th order	+1st order	+2nd order
Subapertured SPO focus (est.)	76 μm	76 μm	76 μm	76 μm	76 μm	76 μm
Focal plane mismatch (rms)	17 μm	17 μm	17 μm	<12 μm	<12 μm	<12 μm
R_{curv} reproducing 0th-order width	4.60×10^4 mm	4.60×10^4 mm	4.60×10^4 mm	2.75×10^4 mm	2.75×10^4 mm	2.75×10^4 mm
Radial ruling mismatch (rms)	N/A	<12 μm	<12 μm	N/A	<12 μm	<12 μm
Mg K linewidth (rms) α	N/A	24 μm	24 μm	N/A	24 μm	48 μm
Expected totals	113 μm	116 μm	116 μm	122 μm	124 μm	131 μm

zeroth-order LSF arising from the patterned grating alone is narrower than the zeroth-order HEW measurement reported, but decoupling the relative contributions of the unpatterned substrate and grating figure cannot be done with the current set of measurements.

5.2 Relative Diffraction Efficiencies

The total number of counts in the LSFs also permits a measurement of the relative intensities of comparable orders. As we do not have knowledge of the total flux incident on the grating, absolute diffraction efficiencies cannot be derived from this data. However, the data do permit an estimate of the relative diffraction efficiencies by measuring the total number of counts in a line over a given exposure time. We calculate efficiency ratios for the +1st and −1st orders of Grating 1, and the +1st and +2nd orders of Grating 2. We also calculate a lower bound on the efficiency ratio between −1st and +1st orders of Grating 2 by calculating the efficiency ratio if all recorded photon events in the −1st Mg K α CCD frame were counts in that line. These measurements are reported in Table 5. An estimate of the diffraction efficiencies relative to the zeroth-order reflection is not possible with the current data set due to the unknown contribution of the unpatterned substrate surrounding the grating to the observed flux.

The measured relative efficiencies reported in Table 5 demonstrate a clear blaze effect from both fabricated gratings. For Grating 1, −1st-order Mg K α is over a factor of 2 brighter than the +1st order, despite the −1st order not being located at the blaze position. The blaze effect is more apparent in Grating 2. We observe an almost complete suppression of Mg K α −1st

order relative to positive orders, and the Mg K α +2nd line, located roughly at the blaze position, is nearly a factor of 2 brighter than the +1st-order line. The concentration of flux at orders higher than ± 1 st serves to increase the signal-to-noise ratio in a more spectrally resolved line and has significance for future x-ray grating spectroscopy missions.

6 Conclusions

Via testing with an SPO at the PANTER x-ray test facility, we have assessed the performance capabilities of two prototype blazed off-plane gratings in the Littrow mounting. The highest resolution demonstrated in these measurements, $R = 800 \pm 20$, is modest compared to the resolutions required of a future x-ray spectrometer. However, the reported resolution does not represent a systematic limit for the fabricated gratings and could be improved by working at higher order, mitigating the figure error of the tested gratings, and/or improving focus quality of the SPO stack. These measurements have also demonstrated a blaze effect from radially ruled off-plane gratings. Via measurements of the relative intensity of diffracted orders, we have shown that the Littrow mounting can be used to effectively suppress orders far from the blaze position and yield greater throughput in higher orders. The demonstration of this blaze capability has implications for the design of future off-plane x-ray grating spectrometers, as it would serve to concentrate flux on one side of the zeroth order, reducing the extent of the detector array required to attain the same signal-to-noise ratio and enabling measurements at high order with greater throughput. However, the technique used in the current work to measure grating efficiencies provides no means of assessing the zeroth-order efficiency with certainty and would be constrained to energies able to be fluoresced by an electron impact source. These limitations motivate the importance of obtaining absolute efficiency measurements at a facility better suited for taking such data, such as a soft x-ray beamline at a synchrotron.

Future measurements of off-plane gratings at beamline facilities like PANTER will greatly benefit from a set of grating aperture masks controlling the illumination of the grating by the focusing optic. The present work employs geometric raytracing in order to estimate the performance of the gratings relative to the SPO PSF. While geometric raytracing is a powerful tool that can be used to better understand the expected changes in the performance of x-ray optics, it is only beneficial while employed

Table 5 The relative diffraction efficiencies for the tested gratings.

Relative efficiencies of diffracted orders		
Grating	Orders compared	Relative efficiency
Grating 1	−1st/ +1st	2.3 ± 0.1
Grating 2	+1st/ −1st	$>43 \pm 10$
	+2nd/ +1st	1.8 ± 0.04

in conjunction with thorough empirical measurements and can still result in ambiguities. Carefully matching the illuminated portion of the SPO to the illuminated portion of the grating via use of an aperture mask will greatly reduce the need to employ numerical methods to disentangle the contributions of alignment, illumination, and fabrication errors and enable easily comparable measurements of the telescope focus and grating orders.

The inference of a significant figure error contribution to the LSFs of both gratings also motivates the need for direct measurements of the grating surface figure. Gross figure error of individual gratings would substantially reduce the performance of a spectrometer employing many co-aligned gratings and, as such, will need to be minimized in future fabrication efforts. Interferometric measurements of the bare fused silica substrate, after UV-NIL replication and after the deposition of the x-ray reflective layer, will help to elucidate the source(s) of the grating deformation inferred in this beamline test. In the event that the fabricated gratings are found to have a figure error smaller than that needed to explain the observed zeroth-order deformation, a new grating module that minimizes mounting stress will be devised for future tests.

In terms of grating fabrication, the next undertaking following this work will be to fabricate large-format, off-plane gratings via the described fabrication procedure. Fabricating large-format gratings will require a new set of nanoimprint molds to be produced. Molds of this size can be made via a commercial process performed by an external vendor. After obtaining these new molds, subsequent gratings can be manufactured over large ($\sim 100 \text{ cm}^2$) formats without changing any of the tooling used to complete the fabrication process described in Sec. 2.2. The blaze angle afforded by (311) Si wafers (29.5 deg) is most similar to the grating facet angles baselined for future missions, and a grating with this blaze angle has already been fabricated (Grating 2). Once a large-format, blazed off-plane grating has been successfully fabricated, characterizing the figure via interferometric measurements and groove facet profile via atomic force microscopy will provide the information necessary to model the anticipated grating performance. Finally, direct performance testing assessing the throughput and resolving power of such a grating will be a substantial step forward for future spectrometers like Arcus and OGRE.

Acknowledgments

We would like to thank the anonymous referees for their helpful suggestions and comments. This work was supported by the NASA Roman Technology Fellowship (NNX12AI16G), a NASA Strategic Astrophysical Technology grant (NNX12AF23G), and a NASA Astrophysics Research and Analysis (APRA) grant (NNX13AD03G). We would also like to recognize the support of the University of Iowa Office of the Vice President for Research as well as the College of Liberal Arts and Sciences. The present work benefits tremendously from the University of Iowa Microfabrication Facility and the University of Iowa Central Microscopy Research Facility, a core resource supported by the Vice President for Research & Economic Development, the Holden Comprehensive Cancer Center and the Carver College of Medicine. Casey DeRoo acknowledges internal funding from the University of Iowa College of Liberal Arts and Sciences. Hearty thanks are due to Wolfgang Burkert and Bernd Budau

at the PANTER x-ray test facility for their invaluable support during the grating test campaign.

References

1. R. K. Smith et al., "Arcus: an ISS-attached high-resolution x-ray grating spectrometer," *Proc. SPIE* **9144**, 91444Y (2014).
2. M. Neviere, P. Vincent, and D. Maystre, "X-ray efficiencies of gratings," *Appl. Opt.* **17**(6), 843 (1978).
3. M. Neviere, D. Maystre, and W. R. Hunter, "On the use of classical and conical diffraction mountings for XUV gratings," *J. Opt. Soc. Am.* **68**(8), 1106 (1978).
4. W. C. Cash, Jr., "X-ray spectrographs using radial groove gratings," *Appl. Opt.* **22**, 3971–3976 (1983).
5. R. Allured and R. T. McEntaffer, "Analytical alignment tolerances for off-plane reflection grating spectroscopy," *Exp. Astron.* **36**, 661–677 (2013).
6. A. E. Franke et al., "Super-smooth x-ray reflection grating fabrication," *J. Vac. Sci. Technol., B* **15**, 2940 (1997).
7. C.-H. Chang et al., "Fabrication of sawtooth diffraction gratings using nanoimprint lithography," *J. Vac. Sci. Technol., B* **21**, 2755 (2003).
8. C.-H. Chang et al., "High fidelity blazed grating replication using nanoimprint lithography," *J. Vac. Sci. Technol., B* **22**, 3260 (2004).
9. R. McEntaffer et al., "First results from a next-generation off-plane x-ray diffraction grating," *Exp. Astron.* **36**, 389–405 (2013).
10. C. T. DeRoo et al., "Pushing the boundaries of x-ray grating spectroscopy in a suborbital rocket," *Proc. SPIE* **8861**, 88611B (2013).
11. V. Burwitz et al., "In focus measurements of IXO type optics using the new PANTER x-ray test facility extension," *Proc. SPIE* **8861**, 88611J (2013).
12. C. Klauber, "Refinement of magnesium and aluminum $K\alpha$ x-ray source functions," *Surf. Interface Anal.* **20**, 703–715 (1993).
13. J. A. Bearden, "X-ray wavelengths," *Rev. Mod. Phys.* **39**(1), 78 (1967).
14. M. Beijersbergen et al., "Silicon pore optics: novel lightweight high-resolution x-ray optics developed for XEUS," *Proc. SPIE* **5488**, 868 (2004).
15. R. Willingale et al., "The hot and energetic universe: the optical design of the Athena+ mirror," (2013)ArXiv e-prints.
16. E. Pfeffermann et al., "The focal plane instrumentation of the ROSAT telescope," *Proc. SPIE* **0733**, 519 (1986).
17. N. Meidinger et al., "CCD detectors for spectroscopy and imaging of x-rays with the eROSITA space telescope," *Proc. SPIE* **7435**, 743502 (2009).
18. K. Dennerl et al., "Determination of the eROSITA mirror half energy width with subpixel resolution," *Proc. SPIE* **8443**, 844350 (2012).
19. W. Cash, "X-ray optics: a technique for high resolution imaging," *Appl. Opt.* **26**, 2915–2920 (1987).
20. P. H. Citrin et al., "Linewidths in x-ray photoemission and x-ray emission spectroscopies: what do they measure?," *Phys. Rev. B* **10**, 1762 (1974).

Casey T. DeRoo is a graduate student at the University of Iowa. He received his Bachelor of Arts degree in physics and classical studies from Concordia College in 2011. His current research interests include optical design, manufacture of optics via microfabrication techniques, and x-ray spectroscopy. He is a member of SPIE.

Randall L. McEntaffer is an associate professor of physics and astronomy at the University of Iowa. He specializes in the design, fabrication, testing, and implementation of x-ray diffraction gratings for high throughput, high resolving power astrophysical observations. His research topics include the fabrication of x-ray gratings using nanofabrication methodologies, alignment and testing of aligned grating modules, and the incorporation of grating modules into space-based spectrometers.

Drew M. Miles is a first-year graduate student at the University of Iowa with a background in space instrumentation. With previous experience on a sounding rocket payload and a CubeSat instrument, he seeks to continue his PhD studies in experimental astrophysics.

Thomas J. Peterson is working on completing BS degrees in mathematics, physics, and astronomy at the University of Iowa. He works

on grating fabrication for the Off-plane Grating Rocket Experiment (OGRE), a suborbital rocket mission designed to test a high-resolution soft x-ray spectrometer. After his undergraduate degree, he will be attending the University of Minnesota, where he will be pursuing his PhD in condensed matter physics.

Hannah Marlowe received her undergraduate degree in astrophysics from Agnes Scott College in 2011. She received her PhD from the University of Iowa as a NASA Earth and Space Science fellow in 2011, working on x-ray diffraction gratings and polarimeters for flight missions.

James H. Tutt completed his PhD at the Open University (UK) in 2012. He continued at the Open University as a postdoctoral research scholar, working on the use of EM-CCDs in medical imaging before moving to the University of Iowa (UI) in 2014. At UI, he is working on a suborbital rocket mission that is designed to test a high resolution soft x-ray spectrometer based on EM-CCD cameras and OGRE.

Benjamin D. Donovan is an undergraduate at the University of Iowa, where he works on grating alignment for the OGRE, a suborbital rocket mission designed to test a high-resolution soft x-ray spectrometer. After he completes his undergraduate degree, he plans on pursuing a graduate degree in astronomy and astrophysics, where he plans on continuing to pursue his interest in astronomical instrumentation.

Ryan Allured is an astrophysicist at the Harvard-Smithsonian Center for Astrophysics. His research interests span a wide array of instrumentation for astronomical x-ray telescopes. He develops mission concepts for next-generation x-ray observatories as well as the optical technologies to enable such missions. Additionally, he investigates the fundamental optical theories relevant to x-ray optics in order to improve optical performance modeling. He received his PhD in physics from the University of Iowa.

Biographies for the other authors are not available.